ACS OMEGA

http://pubs.acs.org/journal/acsodf

Article

Waste PET Plastic-Derived CoNi-Based Metal–Organic Framework as an Anode for Lithium-Ion Batteries

Yaxin Wang, Huimin Wang, Shuyuan Li, and Shaorui Sun*

Cite This: *ACS Omega* 2022, 7, 35180–35190

Read Online

ACCESS | Metrics & More | Article Recommendations | Supporting Information

ABSTRACT: Recycling waste PET plastics into metal–organic frameworks is conducive to both pollution alleviation and sustainable economic development. Herein, we have utilized waste PET plastic to synthesize CoNi-MOF applied to lithium battery anode materials via a low-temperature solvothermal method for the first time. The preparation process is effortless, and the sources' conversion rate can reach almost 100%. In addition, the anode performance of MOFs with various Co/Ni mole ratios was investigated. The as-synthesized $Co_{0.8}$Ni-MOF exhibits excellent crystallinity, purity, and electrochemical performance. The initial discharge and charge capacities are 2496 and 1729 mAh g^{-1}, respectively. Even after 200 cycles, the $Co_{0.8}$Ni-MOF electrode can exhibit a high Coulombic efficiency of over 99%. Consequently, given the environmental and economic benefits, the $Co_{0.8}$Ni-MOF derived from waste PET plastic is thought to be an appealing anode material for lithium-ion batteries.

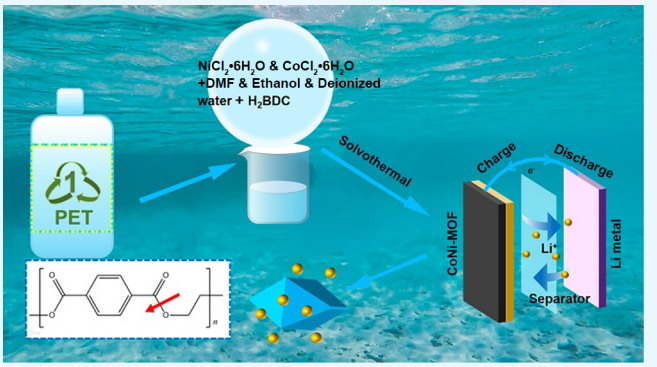

INTRODUCTION

Environmental and energy issues are the two most serious problems of the 21st century.[1−3] Nowadays, demand for energy conversion and storage is increasing as a result of severe environmental pollution caused by the widespread use of fossil fuels and the need to power millions of portable electronics and electric vehicles. The rational use of clean and renewable energy and the development of sustainable energy storage systems (EES) have emerged as global goals for addressing energy and environmental crises.[4−9] Among various energy storage equipment, lithium-ion batteries (LIBs) are the first to be considered owing to qualities such as high energy density, long cycle life, low self-discharge, and environmental friendliness.[10−12] However, commercially available graphitic anodes in LIBs with limited theoretical capacity (370 mAh g^{-1}) cannot meet the ever-increasing demands for high energy densities in electric vehicles and grid-scale energy storage systems.[13−16] As a result, the key to achieving high-energy LIBs is to look for promising anode candidates to replace conventional graphite.

Metal–organic frameworks (MOFs) have appeared as a burgeoning class of porous material consisting of metal nodes and organic linkers.[17,18] Since the synthesis of the first MOFs by Yaghi and Li in the 1990s,[19] they have attracted considerable attention in recent decades due to their intriguing structural diversity and a wide range of potential applications, such as catalysis,[20,21] gas storage and separation,[22,23] sensing,[24,25] drug delivery,[26,27] and a variety of other areas. Recently, many researchers have concentrated their efforts on the design and synthesis of MOFs for clean energy applications such as fuel cells,[28] lithium-ion rechargeable batteries,[10] supercapacitors,[29] and solar cells.[30] In 2009, Tarascon et al. first demonstrated that MOFs (MIL-53 (Fe)) were used as anode materials for lithium storage via a conversion reaction.[31] Since then, because of their structural diversity, customizable redox characteristics, simple synthesis procedures, and low cost, MOFs have emerged as novel electrode materials with significant potential in lithium-ion batteries.[10,32−34] Meanwhile, with regard to MOFs, the metal center has a significant impact on the electrode's lithium storage behavior.[35] Co-based MOFs have been widely used as electrode materials for advanced energy storage applications due to their availability and ease of electron transfer between multiple oxidation states ranging from +1 to +4 during conversion reactions. However, most Co-based MOFs have low conductivity, and this problem has been addressed by incorporating insoluble conductive additives and combining MOFs with conductive matrices (e.g., carbon nanotubes, reduced graphene oxide, conductive polymers, etc.). Additionally, the synthesis of multi-metallic MOFs is also a great alternative for intensifying electronic conductivity. Doping metal ions such as lightweight Li, Mg, Al,

Received: July 6, 2022
Accepted: August 19, 2022
Published: September 20, 2022

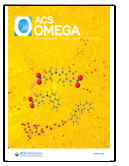

https://doi.org/10.1021/acsomega.2c04264
ACS Omega 2022, 7, 35180−35190

Scheme 1. (a) Preparation Process of CoNi-MOF. (b) Working Principle of the CoNi-MOF/Li Half-Cell. (c) CoNi-MOF with Possible Interaction of Li^+ Ions

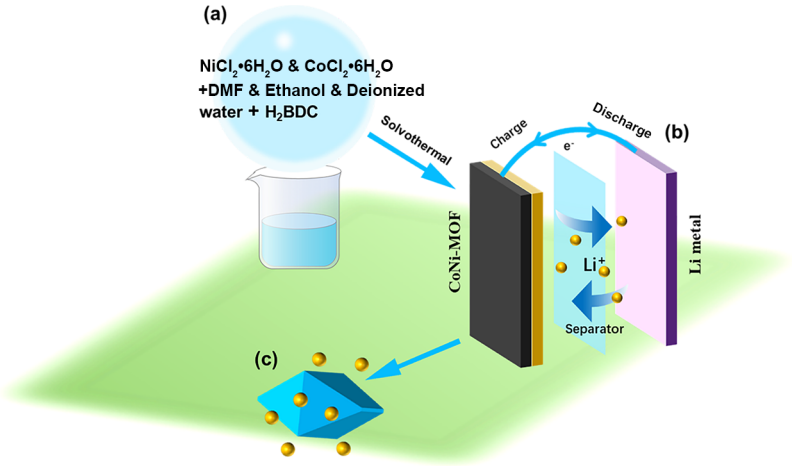

Ni, and Mn into Co-based MOFs could help to conserve cobalt resources while also effectively facilitating electronic coupling between metal nodes to improve material conductivity.[32,36,37] Hu et al. reported a novel bimetallic ZnCo-MOF, and using soft X-ray absorption spectra (sXAS), they demonstrated that bimetallic MOFs could significantly improve electrode performance due to the synergistic effect of Zn^{2+} and Co^{2+}.[38] Additionally, Zhou et al. reported a 2D BP/NiCo MOF via a simple solution reaction route at room temperature using Ni^{2+}, Co^{2+}, and benzene dicarboxylic acid (BDC) as precursors, which demonstrated high reversible capacity and excellent cycling durability as an anode in LIBs.[39] Although tremendous progress has been made in the development of MOF-based lithium electrode materials, there are still many challenges that hinder the practical application of these materials. First, many of the complex organic ligands used in the synthesis of MOFs are expensive and may require a degree of processing complexity. Therefore, large-scale production of MOF materials at a reasonable cost is critical for making them economically viable for industrial applications.

As an important ligand, 1,4-benzenedicarboxylic acid (BDC) has been used to design many MOF system structures.[21] More importantly, it is abundant as a starting material from the recycling of polyethylene terephthalate and the metabolites of aromatic hydrocarbon oxidation.[40] Poly(ethylene terephthalate) (PET) is widely used in packaging and textiles due to its good mechanical properties, low permeability to moisture and gas, and high heat resistance.[40−43] According to statistics, global PET consumption has surpassed 24 million tons (62.8 billion bottles) per year and is continuing to rise. Because of its poor biodegradability, the current common practice of PET waste land filling has caused serious environmental problems. As a result, the innovative use of BDC derived from waste PET for MOF synthesis will not only improve the economics of MOF fabrication but will also reduce the environmental threat associated with waste PET landfilling, ultimately creating a high-value end-use market for PET waste.[44−46]

Herein, we concentrate on a simple and integrated approach to addressing the environmental concern associated with waste PET bottles by recycling them into promising lithium anode materials in the form of CoNi-MOF. Moreover, we also reported the solvothermal synthesis of CoNi-MOF with various Co/Ni ratios (the molar ratios of Co/Ni are 0.5:1, 0.8:1, and 1:1) to select the optimal MOF as the LIB anode material. Among them, the as-synthesized $Co_{0.8}$Ni-MOF exhibits excellent crystallinity, purity, and electrochemical performance with superior cyclic stability. To the best of our knowledge, there is no literature report that efficiently recycles waste PET into CoNi-MOF as an anode for LIBs. Thus, it is firmly believed that the waste PET plastic-derived $Co_{0.8}$Ni-MOF has great potential as an electrode material and would be beneficial to the mitigation of global warming as well as the circular construction of the economy.

EXPERIMENTAL SECTION

Chemicals and Regents. Cobaltous chloride hexahydrate ($CoCl_2·6H_2O$, 99.5%), terephthalic acid (BDC, 98%), and nickel chloride hexahydrate ($NiCl_2·6H_2O$, 95%) were bought from Sinopharm. Ethylene glycol (EG, 99.8%), ethanol (95%), and *N*,*N*-dimethylformamide (DMF, 99.8%) were purchased from Aladdin. No further purification was performed on any of the reagents. The raw material was clear mineral water bottles (PET plastics) collected from domestic waste. All of the experiments in this work were conducted using deionized water.

Synthesis of BDC. The process schematic for the synthesis of terephthalic acid derived from PET according to reference is illustrated in Scheme S1.[47] Briefly, the clear mineral water bottles' labels and caps were removed, and the bottles were cut into small pieces. The small flakes were washed with water and soap before being dried in an oven at 60 °C overnight. Then, the PET hydrolysis experiment was carried out in a stainless-steel autoclave lined with Teflon. PET flakes (2.5 g) were placed in the autoclave along with 5 mL of ethylene glycol (EG) and 50 mL of H_2O, and the reactor was heated to 210 °C and kept there for 8 h. After the reaction, the product was centrifuged, washed twice with ethanol, and dried at 80 °C for 12 h.

Synthesis of CoNi-MOF. As shown in Scheme 1, the CoNi-MOF was synthesized via solvothermal methods in a Teflon-lined high-pressure reactor. First, 10 mL of DMF, 10 mL of ethanol, and 10 mL of deionized water were combined in a beaker. Second, 7.2 mmol of BDC (the metal's molar ratio to BDC is 1.05) was added to the above mixture, and the solution was sonicated for 15 min to achieve a uniform

https://doi.org/10.1021/acsomega.2c04264
ACS Omega 2022, 7, 35180−35190

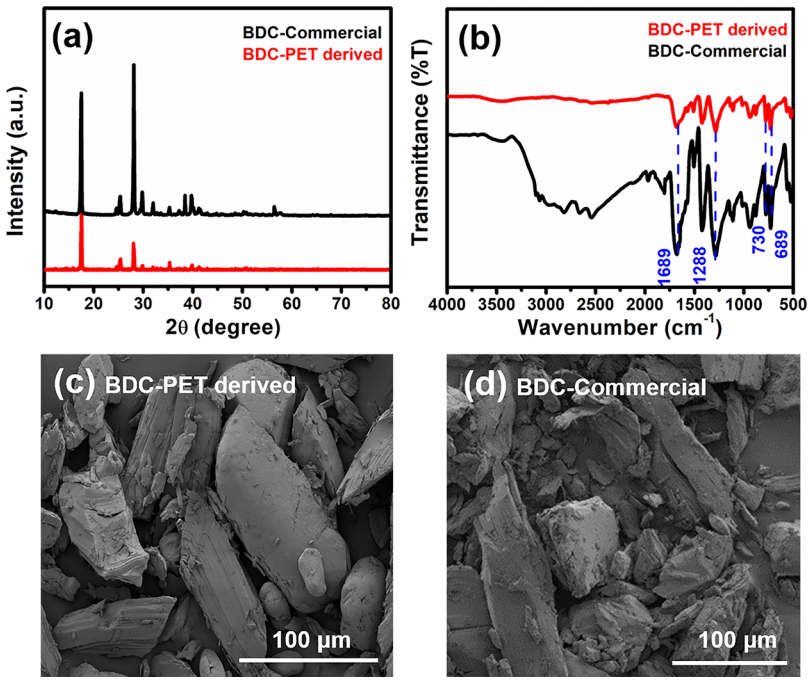

Figure 1. (a) XRD patterns, (b) FTIR infrared spectra, and SEM images (c, d) of the PET-derived BDC and commercial BDC.

suspension. Third, 3.02 mmol of $NiCl_2{\cdot}6H_2O$ and 3.78 mmol of $CoCl_2{\cdot}6H_2O$ were added to the solution and sonicated for 15 min until completely dissolved. Then, the above solution was transferred into a 50 mL Teflon-lined stainless steel autoclave and heated at 150 °C for 24 h. Finally, the product was obtained via centrifugation, washed with DMF and ethanol five times, and then dried in a vacuum oven overnight at 60 °C. In comparison, CoNi-MOF materials ($Co_{0.5}$Ni-MOF and $Co_{1.0}$Ni-MOF) were, respectively, synthesized by adding different Co/Ni molar ratios (such as 0.5:1 and 1:1) to the solution.

Material Characterization. X-ray powder diffraction (XRD) measurements were taken using a PAN analytical X-ray diffractometer (Cu Kα source, λ = 1.54178 Å). X-ray Rietveld refinement was performed with the FullProf Software package. The scanning electron microscopy images were obtained via a Carl Zeiss Ultrafield-emission scanning electron microscopy (FESEM) unit equipped with energy-dispersive spectroscopy (EDS). The materials' morphology and microstructure were examined further using transmission electron microscopy (TEM; JEOL-JEM-2100F). Fourier transform infrared spectroscopy (FTIR) was performed with a PerkinElmer (Spectrum 2) spectrophotometer at a resolution of 4 cm^{-1} in the scanning range of 400−4000 cm^{-1}. The thermal stabilities of the samples were determined using the TA Instruments SDT650 thermogravimetric analysis (TGA) method. N_2 adsorption−desorption studies were performed using the Brunauer−Emmett−Teller (BET) method via a Quantachrome Nova 2000e BET analyzer. The Co/Ni ratio in the CoNi-MOF was analyzed by inductively coupled plasma-atomic emission spectrometry (ICP-AES) using IRIS Intrepid II XSP (Thermo Fisher Scientific). X-ray photoelectron spectroscopy (XPS) spectra were obtained using a Thermo Fisher Scientific ESCALAB250Xi spectrometer. ^{1}H NMR and ^{13}C NMR spectra were provided via a Bruker spectrometer (MSL 400).

Electrochemical Measurements. Electrochemical tests were performed on coin-type cells (size: 2025), which were made up of a working electrode and a lithium foil counter electrode separated by a Celgard 2400 microporous membrane. The active materials, carbon black (super P) and poly vinylidene difluoride (PVDF), were dissolved in *N*-methyl pyrrolidinone (NMP) in a weight ratio of 7:2:1. The resulting slurry was cast on Cu foil and dried in a vacuum at 100 °C for 10 h. The cell assembly was carried out in a glove box filled with argon (H_2O, O_2 < 0.5 ppm). The electrolyte used was 1 M $LiPF_6$ in a 1:1 volume ratio of ethylene carbonate (EC) and dimethyl carbonate (DMC). The cells were galvanostatically charged and discharged at different rates using multichannel Neware battery testing equipment in a voltage cutoff range of 0.01−3 V for cycle and rate performance. An electrochemical workstation (CHI 660a) was used to do CV measurements at a scan rate of 0.2 mV s^{-1}. Electrochemical impedance spectra (EIS) were also measured in the frequency range of 10^5 to 10^{-2} Hz on a CHI 660a electrochemical workstation.

RESULTS AND DISCUSSION

Characterization of PET-Derived BDC. The XRD patterns (Figure 1a) ensure that the peaks of PET-derived BDC are positioned at 2θ = 17.4, 25.3, and 28°, which are characteristically identical to the commercial sample and reported literature.[48] From Figure 1b, both FTIR spectra show the same characteristic peaks. Aromatic ring characteristic peaks are observed at 730 and 689 cm^{-1}, which are assigned to ringing-and-out-of-plane bending vibrations of aromatic rings,[49] whereas the peaks for carboxylic groups are located at 1288, 1420, 1689, 2542, and 2657 cm^{-1}. The band at 1689 cm^{-1} denotes the C═O stretching vibration of carbonyl groups, and the peak at 1288 cm^{-1} is attributed to the C−O symmetric stretching, as per characteristic IR absorption frequencies of organic functional groups. This indicates that the obtained product was indeed BDC, as evidenced by the spectrum's similarity to commercial BDC. The FESEM

https://doi.org/10.1021/acsomega.2c04264
ACS Omega 2022, 7, 35180−35190

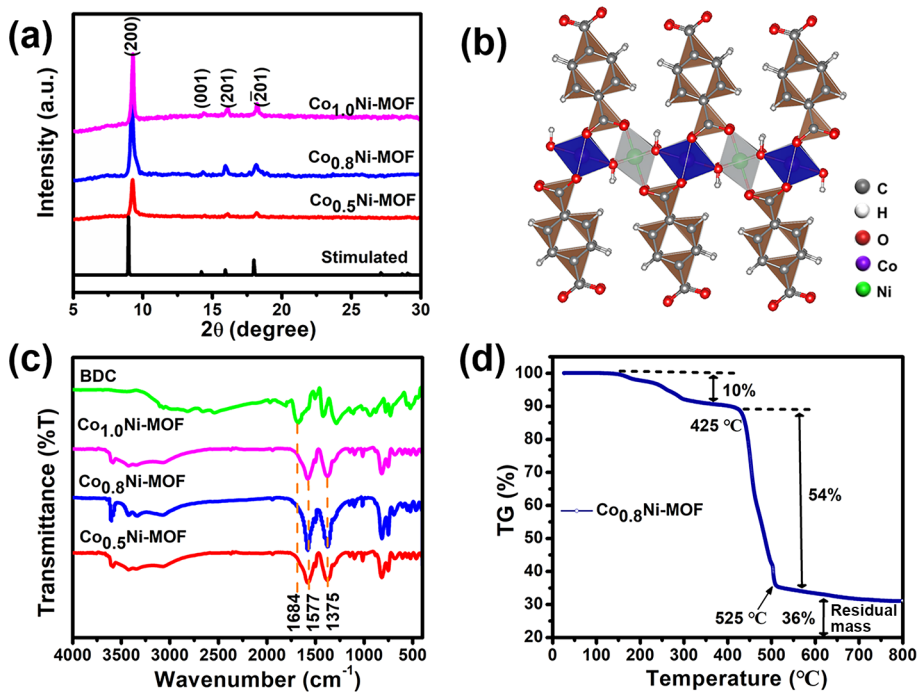

Figure 2. (a) PXRD patterns, (b) crystal structure of CoNi-MOF, (c) FTIR infrared spectra of CoNi-MOF synthesized from PET-derived BDC, and (d) TGA curves of $Co_{0.8}$Ni-MOF.

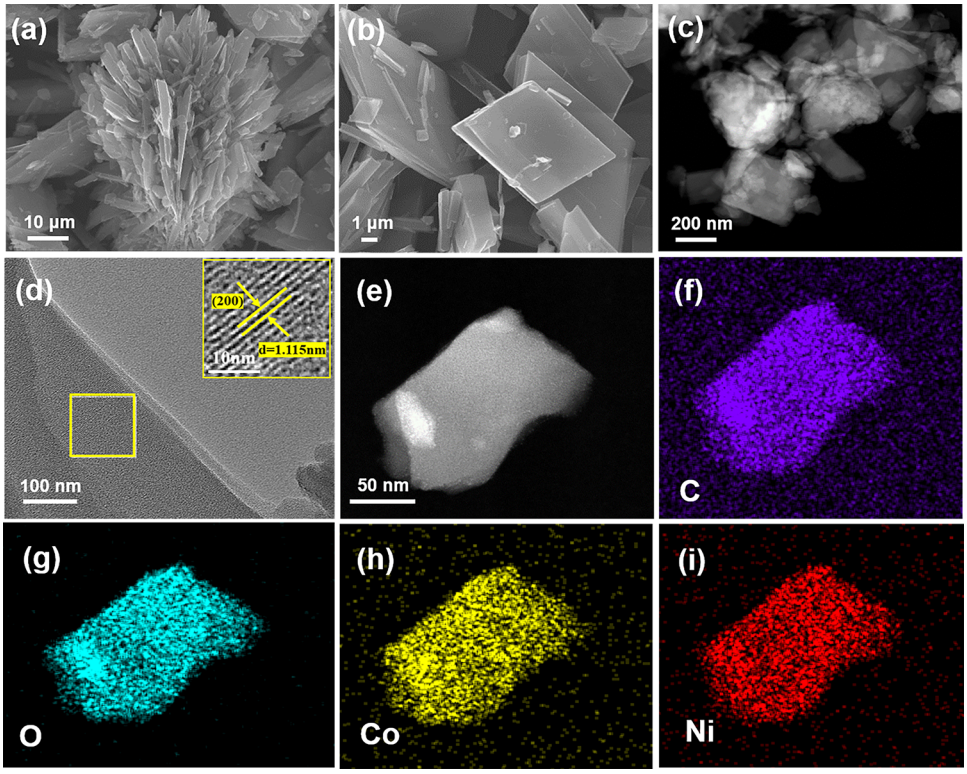

Figure 3. (a, b) SEM images, (c, e) TEM images, and (d) HRTEM image of $Co_{0.8}$Ni-MOF; (f–i) TEM-EDS mapping images of $Co_{0.8}$Ni-MOF: (f) C, (g) O, (h) Co, and (i) Ni elements.

analysis (Figure 1c,d) reveals that both PET-derived BDC and commercially available BDC have a similar morphology. The ^{1}H NMR and ^{13}C NMR spectra of the PET-derived BDC shown in Figure S1 confirm that the product does not require purification. The PET-derived BDC also exhibits an identical TGA curve to the commercial BDC (Figure S2).

Characterization of CoNi-MOF. The crystallinity, phase analysis, and structural properties of MOF samples prepared at different molar ratios of Co/Ni were examined by powder X-ray diffraction (XRD), as shown in Figure 2a and Figure S3. All the CoNi-MOF XRD patterns are isostructural to the previously reported Ni-based MOFs (no. 985792).[50] There-

https://doi.org/10.1021/acsomega.2c04264
ACS Omega 2022, 7, 35180−35190

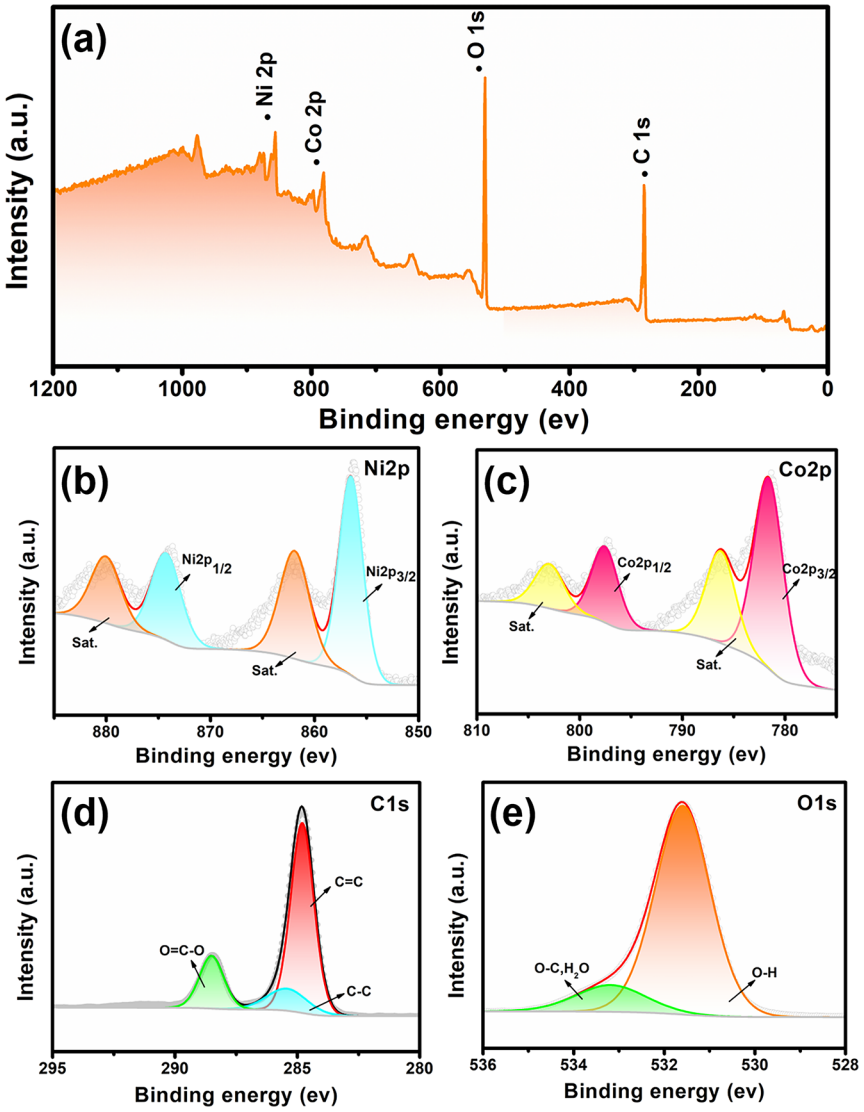

Figure 4. (a) Wide-range XPS spectrum of $Co_{0.8}$Ni-MOF. (b) XPS survey spectrum of Ni 2p and the corresponding XPS spectra of (c) Co 2p, (d) C 1s, and (e) O 1s.

fore, the atomic arrangement inside CoNi-MOF can be successfully defined (Figure S4 and Table S1). Four sharp peaks appearing at 2θ = 9.219, 14.302, 15.959, and 18.161° and matching well with the relevant crystal faces are (200), (001), (201), and (−201), respectively, indicating the formation of pure products. Furthermore, as the Co/Ni molar ratio increases from 0.5 to 1.0, the characteristic peak intensity is enhanced. This can be attributed to the crystalline enhancement and size growth of CoNi-MOF,[51] which will be discussed in the following. All the XRD patterns indicate that these frameworks have similar structures, as shown in Figure 2b. Six O atoms coordinate both the Co and Ni atoms, and these pseudo octahedra are further edge/corner-connected with each other in the (200) crystallographic plane along the [010]/[001] direction to form 2D bimetal layers separated by BDC molecules.[52] Furthermore, Figure 2c displays the FTIR spectra of all samples of CoNi-MOF synthesized from PET. It can be seen that there is a wide band at 3580−3400 cm^{-1}, indicating the presence of hydroxyl and water molecules,[53] and for comparison, the corresponding FTIR spectrum for 1,4-H_2BDC is also shown. The reaction of 1,4-H_2BDC with Co^{2+} and Ni^{2+} results in complete deprotonation by the disappearance of the nonionized carboxyl group's characteristic bands (νC═O, 1684 cm^{-1}). New bands can be observed in the regions of 1672−1508 cm^{-1} ascribed to carboxylate group asymmetric stretching vibrations, whereas bands in the 1444−1375 cm^{-1} range can be attributed to symmetric stretching.[54] These new bands suggest that the Co^{2+} and Ni^{2+} ions have successfully interacted with the 1,4-H_2BDC ligands. The TGA analysis determined the thermostability of all CoNi-MOF samples in a temperature range of 25−800 °C (Figure 2d and Figure S5). All samples exhibit good thermal stability and still maintain their structural integrity at a temperature of 375 °C. There is a significant decrease at around 375−525 °C, which is due to the thermal degradation of MOF.[51] In the case of $Co_{0.8}$Ni-MOF, at temperatures ranging from 25 to 350 °C, an initial weight loss of 10% was observed due to the release of DMF and ethanol molecules. The next weight loss of approximately 54% may result from the decomposition of the main skeleton of $Co_{0.8}$Ni-MOF and the gasification of ligands at temperatures ranging from 425 to 525 °C. The

https://doi.org/10.1021/acsomega.2c04264
ACS Omega 2022, 7, 35180−35190

residual mass of the product after a complete pyrolysis reduction at 525 °C was 36%.

The morphologies of MOFs synthesized at different Co/Ni molar ratios were analyzed by SEM at different magnifications, as presented in Figure 3a,b and Figure S6. The $Co_{0.8}$Ni-MOF has a micrometer-sized dandelion-like morphology composed of bulks with a length of 6−10 μm, as shown in Figure 3a,b. The assembled bulk-like framework of the $Co_{0.8}$Ni-MOF can also be apparently observed in the TEM image in Figure 3c, which could lead to improved electrolyte accessibility by forming an ion-buffering reservoir and thus shortening the Li^+ diffusion length to the interior surfaces.[55] Furthermore, the HRTEM image in Figure 3d shows very clear crystalline planes with d-spacings of 1.115 nm, which can be ascribed to the (200) planes of $Co_{0.8}$Ni-MOF. The chemical composition of $Co_{0.8}$Ni-MOF was also investigated using energy-dispersive spectroscopy (EDS), as presented in Figure 3f−i. The EDS pattern of the $Co_{0.8}$Ni-MOF shows that the elements C, O, Co, and Ni are uniformly distributed throughout the sample, indicating that the $Co_{0.8}$Ni-MOF was successfully formed. Figure S6 also includes SEM images of the $Co_{0.5}$Ni-MOF and $Co_{1.0}$Ni-MOF samples. The morphology of the MOF samples changes from bowknot-like (Figure S6a) to dandelion-like (Figure 3a) and then to flower-like (Figure S6c). When the molar ratio of Co/Ni is 0.5:1, as shown in Figure S6b, relatively small bulk structures are formed first, and then, with the increase in Co/Ni molar ratio, the smaller bulks gradually develop into larger bulks. Figures S7 and S8 represent the SEM−EDX mapping images of $Co_{0.5}$Ni-MOF and $Co_{1.0}$Ni-MOF, respectively, which also clearly support that, in the sample, all elements are distributed uniformly. Inductively coupled plasma-atomic emission spectrometry (ICP-AES) elemental analysis demonstrated that the atomic ratios of Co/Ni in Co*x*Ni-MOF (x = 0.5, 0.8, and 1.0) are calculated to be 0.46, 0.75, and 0.96, respectively (Figure S9 and Table S2). These observations are in accordance with the molar ratios of the initial feeding materials, further revealing the successful preparation of the Co*x*Ni-MOF.

As shown in Figure 4, the XPS technique was used to investigate the chemical composition and oxidation states of $Co_{0.8}$Ni-MOF. Figure 4a indicates the existence of Ni, Co, C, and O elements. The high-resolution Ni 2p spectra (Figure 4b) display two primary peaks centered at 856.3 and 874.0 eV, respectively, which are ascribed to Ni $2p^{3/2}$ and Ni $2p^{1/2}$, as well as two matching satellite peaks positioned at 861.4 and 879.6 eV, demonstrating the presence of Ni^{2+} in the $Co_{0.8}$Ni-MOF.[35] Further, the high-resolution Co 2p XPS spectrum of the as-synthesized $Co_{0.8}$Ni-MOF can also be seen in Figure 4c. Two distinct peaks appear at binding energies of 781.54 eV for Co $2p^{3/2}$ and 797.49 eV for Co $2p^{1/2}$, with two pronounced satellite peaks (786.44 and 803.11 eV, respectively) beside them, illustrating that Co ions are predominantly in the Co^{2+} state.[33] Notably, the coexisting Ni^{2+} and Co^{2+} cations in the $Co_{0.8}$Ni-MOF supply multiple active sites for lithium storage. In addition, C═C, C−C, and O═C−O are attributed to three peaks (Figure 4d) centered at 284.5, 285.3, and 288.5 eV, respectively. The O 1s spectrum (Figure 4e) could be separated into two peaks, positioned at 531.5 and 532.6 eV, respectively, owing to hydroxyl and chemisorbed water. Finally, by using the XPS technique, the atomic content ratio of Co and Ni in the $Co_{0.8}$Ni-MOF could be identified to be 0.72:1.

Figure 5 and Figure S10 present the N_2 adsorption−desorption isotherms and the corresponding Barrett−Joyner−

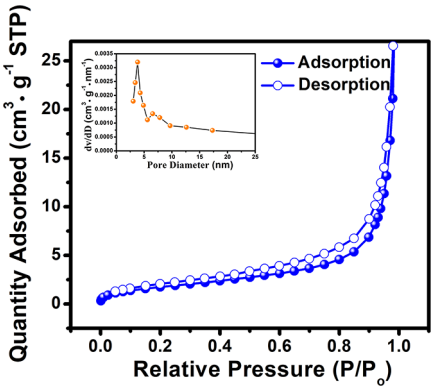

Figure 5. N_2 adsorption−desorption isotherm of $Co_{0.8}$Ni-MOF. The inset shows the BJH pore size distribution curve.

Halenda (BJH) pore size distribution profiles of the CoNi-MOF. The results are summarized in Table S3. All of the CoNi-MOF samples exhibit a typical type-II sorption isotherm with an H_4-type hysteresis loop, indicating that they are mesoporous. As depicted in Figure 5, the as-calculated Brunauer−Emmett−Teller (BET) specific surface area and total pore volume for $Co_{0.8}$Ni-MOF are 13.688 and 0.055 cm^3 g^{-1}, respectively, demonstrating that the $Co_{0.8}$Ni-MOF has low porosity. Furthermore, previous research has also reported MOFs with low porosity.[39,56] The ultrahigh specific surface of the electrode materials frequently results in superfluous side reactions with the electrolyte, particularly at low potentials (vs Li/Li^+), causing the LIB's performance to deteriorate.[55] As a result, the as-synthesized low CoNi-MOF's BET specific surface area may be advantageous.

Electrochemical Measurements. To assess the electrochemical performance of the $Co_{0.8}$Ni-MOF as-prepared for Li-ion storage, the first three successive CV scans of $Co_{0.8}$Ni-MOF at a scan rate of 0.2 mV s^{-1} in the potential range of 0.01−3.0 V vs Li/Li^+ are shown in Figure 6a. The initial cathodic scan illustrates two distinct cathodic peaks at 0.625 and 0.95 V, which belong to the Li-ion intercalation $Co_{0.8}$Ni-MOF. A sloppy peak at 1.05 V (lithiation) disappears in the subsequent scans, which is attributed to the establishment of the SEI layer at the electrode/electrolyte interface.[57] The anodic peaks at 0.825 and 1.25 V are caused by the delithiation reaction of $Co_{0.8}$Ni-MOF. In the following successive cycles, the weak peaks at 0.615 and 1.15 V may be related to the reversible insertion and deintercalation of Li ions into the benzene ring and carboxylic acid groups of the $Co_{0.8}$Ni-MOF framework.[49] After the first electrochemical cycle, the CV curves of subsequent cycles almost overlap, indicating good cycling stability and reversibility of $Co_{0.8}$Ni-MOF. The galvanostatic charge/discharge profiles of the $Co_{0.8}$Ni-MOF for various cycles within the potential window of 3.0−0.01 V vs Li/Li^+ and at a current density of 0.5 A g^{-1} are shown in Figure 6b. The initial discharge and charge capacities are 2496 and 1729 mAh g^{-1}, respectively, corresponding to a Coulombic efficiency (CE) of 69.27%, indicating a significant initial irreversible reaction caused by the formation of an SEI (surface electrolyte interface) film on the electrode surface and electrolyte decomposition.[59] During the first discharge process, three plateaus can be seen around 1.25, 0.95, and 0.55 V,

https://doi.org/10.1021/acsomega.2c04264
ACS Omega 2022, 7, 35180−35190

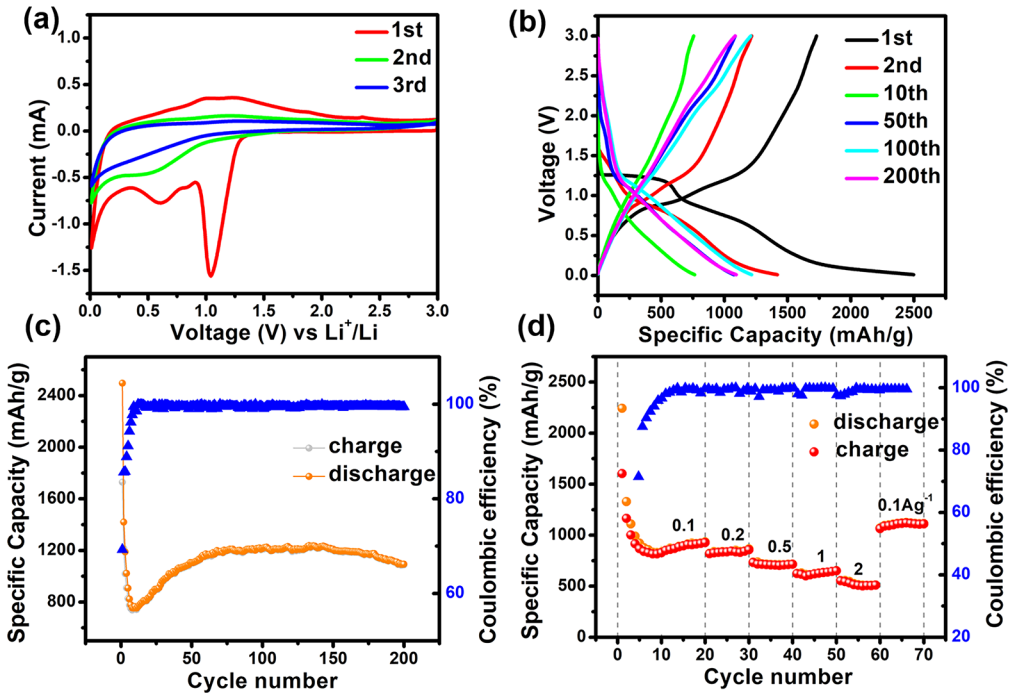

Figure 6. Electrochemical performance of the as-synthesized $Co_{0.8}$Ni-MOF: (a) Cyclic voltammograms (CVs) at a scan rate of 0.2 mV s^{-1}. (b) Galvanostatic charge−discharge profiles at a current density of 500 mA g^{-1}. (c) Cycling performance and Coulombic efficiency at a current density of 500 mA g^{-1}. (d) Rate performance at different current densities from 0.1 to 2.0 A g^{-1}.

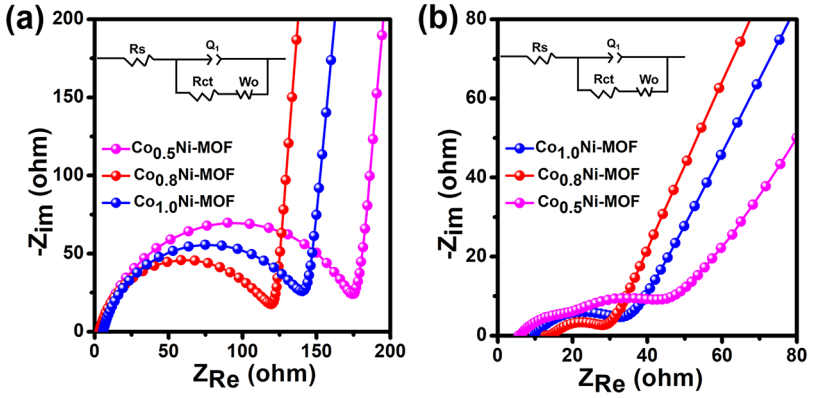

Figure 7. Nyquist plots of all samples (a) at a pristine state and (b) after 200 continuous cycles at 0.5 A g^{-1}. Inset: the equivalent circuit models used to fit impedance data.

which are consistent with the CV results mentioned above, suggesting the same Li^+ ion insertion mechanisms. Although there is a decrease in reversible capacity values for the first few cycles, a nearly invariable capacity of 1419 mAh g^{-1} is obtained in the following cycles. Moreover, the charge−discharge curves of $Co_{0.8}$Ni-MOF are comparable from the 100th to the 200th cycle, which demonstrates its stable electrochemical performance during continuous intercalation and deintercalation of Li ions. Furthermore, Figure S11 shows that the galvanostatic discharge and charge profiles of $Co_{0.5}$Ni-MOF and $Co_{1.0}$Ni-MOF are similar for $Co_{0.8}$Ni-MOF under 500 mA g^{-1} in the first cycling processes, indicating that the same redox reactions are occurring during the electrochemical processes. It was also found that both $Co_{0.5}$Ni-MOF and $Co_{1.0}$Ni-MOF presented smaller discharge (charge) capacities than $Co_{0.8}$Ni-MOF. The discharge (charge) capacities of $Co_{0.5}$Ni-MOF and $Co_{1.0}$Ni-MOF are 1768 (1056) and 2036 (1254) mAh g^{-1}, resulting in Coulombic efficiency (CE) values of 59.74 and 61.61%, respectively. Figure 6c and Figure S12a exhibit the cycling behavior of all CoNi-MOF samples. It is obvious that $Co_{0.8}$Ni-MOF maintains its capacity advantage over other samples. A reversible capacity of 1200 mAh g^{-1} is retained after 200 cycles, which is much higher than those of $Co_{0.5}$Ni-MOF (750 mAh g^{-1}) and $Co_{1.0}$Ni-MOF (900 mAh g^{-1}). Even after 200 cycles, the $Co_{0.8}$Ni-MOF electrode can exhibit a high CE of over 99%, as shown in Figure 6c. The improved Li^+ diffusion kinetics during repeated lithiation and delithiation,[51] a gradual activation process could be attributed to the stable cycling performance. As summarized in Figure 6d and Figure S12b, $Co_{0.8}$Ni-MOF also shows the most outstanding rate property among all CoNi-MOF samples. When cycled at 0.1, 0.2, 0.5, 1, and 2 mA g^{-1}, the $Co_{0.8}$Ni-MOF electrode delivers average charge capacities of 914, 830, 713, 620, and 516 mAh g^{-1}, respectively. More importantly, the capacity is increased to 1113 mAh g^{-1} after lowering the current rate back to 0.1 A g^{-1}. This may be due to the activation caused by higher-rate

https://doi.org/10.1021/acsomega.2c04264
ACS Omega 2022, 7, 35180−35190

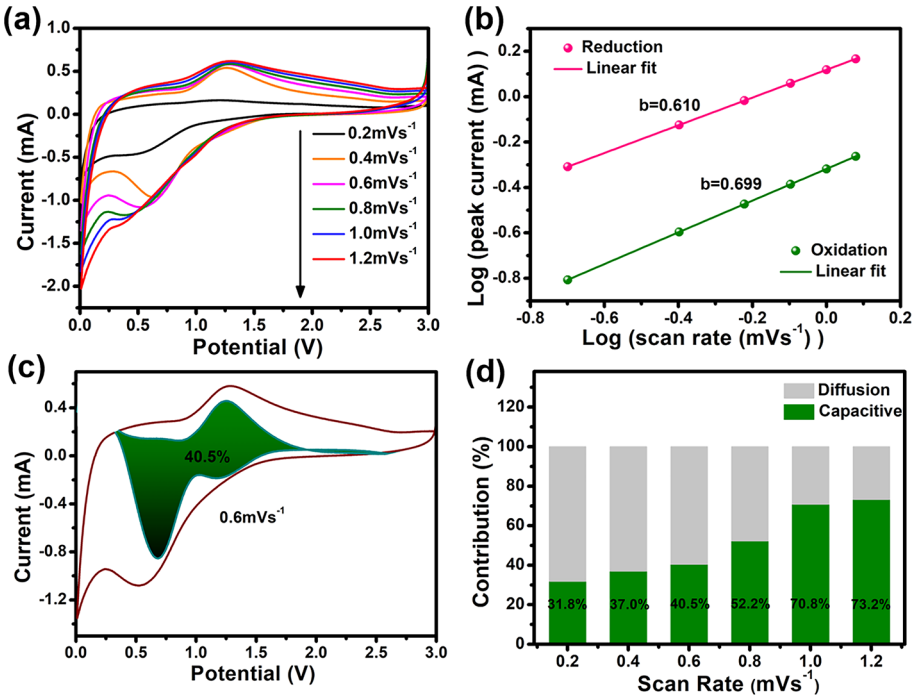

Figure 8. Kinetics of the electrochemical behavior toward Li^+ for the $Co_{0.8}$Ni-MOF electrode: (a) CV curves at various scan rates ranging from 0.2 to 1.2 mV s^{-1}. (b) Relationship between peak currents and potential swing rates. (c) Separation of capacitive and diffusion currents to the total at 0.6 mV s^{-1} scanning speed. (d) Charge contribution ratios of capacitive and diffusion-controlled devices at various scan rates.

discharging/charging cycles, illustrating the MOF structure's robustness in the face of abrupt current changes. $Co_{0.5}$Ni-MOF and $Co_{1.0}$Ni-MOF, on the other hand, only provide 531 and 401 mAh g^{-1} at 1 A g^{-1}, respectively, and 276 and 198 mAh g^{-1} at 2 A g^{-1}, respectively (Figure S12b). When the current density is restored to 0.1 A g^{-1}, the capacities of $Co_{0.5}$Ni-MOF and $Co_{1.0}$Ni-MOF are restored to 945 and 825 mAh g^{-1}, respectively, which are basically the same as the initial capacitance of the samples. This shows that, after repeated charging and discharging at different current densities, the overall structure of MOFs is not damaged and still has excellent lithium storage performance, which may be due to the inherent characteristics of CoNi-MOF. On the basis of the above discussion, we speculate that $Co_{0.8}$Ni-MOF as an anode material for Li-ion batteries has great potential, even in the previously reported MOFs (Table S4).

Additionally, all CoNi-MOF samples were tested by electrochemical impedance spectroscopy (EIS) before and after 200 cycles at 0.5 A g^{-1} to further understand their electrochemical behaviors. An equivalent circuit model was used to fit the impedance data (Figure 7), and the fitting parameters are summarized in Table S5. All cells exhibit a depressed semi-circle in the high-frequency region, which corresponds to the electrode's charge transfer resistance (R_{ct}), and an inclined line at the low frequency, which corresponds to the Warburg diffusion process (Z_w). Internal resistance is correlated with the intersection of the semi-circle at the real axis in the high-frequency region (denoted as R_s). Both the charge-transfer resistance (R_{ct}) in the high-frequency region and the Warburg impedance in the low-frequency region of $Co_{0.8}$Ni-MOF are smaller than those of $Co_{0.5}$Ni-MOF and $Co_{1.0}$Ni-MOF, indicating that the $Co_{0.8}$Ni-MOF hybrid has a large electrode/electrolyte contact area and accelerated charge transfer and Li^+ diffusion, as shown in Figure 7a. The Nyquist plots of all samples after 200 cycles are shown in Figure 7b, which presents the same order as before cycling. Taking $Co_{0.8}$Ni-MOF as an example, the solution resistance (R_s) increases slightly from 3.126 Ω in the pristine state to 10.72 Ω, signifying its great stability, and the R_{ct} also decreases from 110.2 to 21.1 Ω after 200 cycles, showing the enriched wettability and better connectivity of the electrodes. Furthermore, the Li^+ ion diffusion coefficient of the three electrodes is also compared to demonstrate the electrochemical behaviors mentioned above, as presented in Figure S13.

To better understand the possible reasons for the excellent performance, the reaction kinetics of $Co_{0.8}$Ni-MOF (Figure 8a) at different scan rates ranging from 0.2 to 1.2 mV s^{-1} were analyzed using the following equation: $\log i = \log a + b \log v$, where i is the peak current, v is the scan rate, a is a constant, and b is a function variable parameter. When b approaches 1, the nanofaradaic pseudocapacitance takes over. When b approaches 0.5, the system is said to be Li^+ ion diffusion-controlled.[33,58] As shown in Figure 8b, the calculated values of b at the oxidation and reduction peaks are 0.610 and 0.699, respectively, indicating that the electrochemical reaction of $Co_{0.8}$Ni-MOF was related to capacitive and diffusion behaviors. Furthermore, Trasatti's equation $Q(v) = Qs + Qb = Qs + k(v^{1/2})$ distinguishes the surface charge contribution (Qs) and the bulk diffusion contribution (Qb).[59] It can be seen from Figure 8c that the diffusion-controlled contribution is 40.5% at a scan rate of 0.6 mV s^{-1}, and the capacitive contribution of $Co_{0.8}$Ni-MOF increases with the scan rate, as shown in Figure 8d. When the sweep rate is increased from 0.2 to 1.2 mV s^{-1}, the capacitive contribution also increases from 31.82 to 73.2%. Therefore, the excellent electrochemical performance of $Co_{0.8}$Ni-MOF can be partly attributed to the pseudocapacitive behaviors, which occupied a significant portion of the redox processes, leading to high capacity and rate performance.

https://doi.org/10.1021/acsomega.2c04264
ACS Omega 2022, 7, 35180−35190

CONCLUSIONS

In this work, by using a one-pot solvothermal method, we successfully recovered PET plastic waste as a precursor to fabricate value-added CoNi-MOF and investigated lithium anodic performance for the first time. The as-synthesized $Co_{0.8}$Ni-MOF exhibits excellent crystallinity, purity, and electrochemical performance. The initial discharge and charge capacities are 2496 and 1729 mAh g^{-1}, respectively. Even after 200 cycles, the $Co_{0.8}$Ni-MOF electrode can exhibit a high CE of over 99%. Furthermore, the $Co_{0.8}$Ni-MOF shows excellent rate performance at various rates. The CV curves show excellent overlap and reproducibility, indicating great reversibility and cycling stability of the $Co_{0.8}$Ni-MOF. Altogether, given the environmental and economic benefits, the $Co_{0.8}$Ni-MOF derived from PET waste is thought to be an appealing material for a variety of potential practical applications. Furthermore, compared with the initial CE of most commercial anodes, the first efficiency of $Co_{0.8}$Ni-MOF is still slightly lower. However, this problem has yet to be overcome. Surface coating and prelithiation may provide ideas to solve this problem and improve the overall performance of MOF anodes. Once this problem is solved, lithium anode materials can be easily produced on a large scale in the future and can be explored in other lithium-related fields.

ASSOCIATED CONTENT

Supporting Information

The Supporting Information is available free of charge at https://pubs.acs.org/doi/10.1021/acsomega.2c04264.

Schematic illustration of the preparation process of terephthalic acid derived from PET; table of X-ray Rietveld refinement results for $Co_{0.8}$Ni-MOF; table of ICP-AES analyses of CoNi-MOF; table of summarized BET surface areas, pore volumes, and mean pore diameters of the as-synthesized CoNi-MOF; table of MOFs as the anode material for LIBs; table of comparison of the R_s and R_{ct} of the CoNi-MOF electrodes obtained by fitting with the equivalent circuit; ^{1}H NMR spectra and ^{13}C NMR spectra of the PET-derived BDC; TGA curves of the PET-derived BDC and commercial BDC, $Co_{0.5}$Ni-MOF, and $Co_{1.0}$Ni-MOF; Rietveld refinement of the PXRD pattern of $Co_{0.8}$Ni-MOF; SEM and elemental mapping images of $Co_{0.5}$Ni-MOF and $Co_{1.0}$Ni-MOF; the results of ICP for CoNi-MOF; N_2 adsorption−desorption isotherm of $Co_{0.5}$Ni-MOF and $Co_{1.0}$Ni-MOF; galvanostatic charge−discharge profiles in the first cycle for $Co_{0.5}$Ni-MOF and $Co_{0.8}$Ni-MOF; cycling performance and rate performance of $Co_{0.5}$Ni-MOF and $Co_{1.0}$Ni-MOF electrodes; and variations and fitting images of Z_{re} and $\omega^{-1/2}$ in the low-frequency region of $Co_{0.5}$Ni-MOF, $Co_{0.8}$Ni-MOF, and $Co_{1.0}$Ni-MOF (PDF)

AUTHOR INFORMATION

Corresponding Author

Shaorui Sun − *Beijing Key Laboratory for Green Catalysis and Separation, The Faculty of Environment and Life, Beijing University of Technology, Beijing 100124, PR China;* orcid.org/0000-0001-5891-1956; Email: sunsr@bjut.edu.cn

Authors

Yaxin Wang − *Beijing Key Laboratory for Green Catalysis and Separation, The Faculty of Environment and Life, Beijing University of Technology, Beijing 100124, PR China*

Huimin Wang − *Beijing Key Laboratory for Green Catalysis and Separation, The Faculty of Environment and Life, Beijing University of Technology, Beijing 100124, PR China*

Shuyuan Li − *Beijing Key Laboratory for Green Catalysis and Separation, The Faculty of Environment and Life, Beijing University of Technology, Beijing 100124, PR China*

Complete contact information is available at: https://pubs.acs.org/10.1021/acsomega.2c04264

Notes

The authors declare no competing financial interest.

ACKNOWLEDGMENTS

This work was supported by the National Natural Science Foundation of China (NSFC 21676004). The first author would like to thank Yongheng Si and Yahui Wang for fruitful discussions.

REFERENCES

(1) Tan, X.; Wu, Y.; Lin, X.; Zeb, A.; Xu, X.; Luo, Y.; Liu, J. Application of MOF-Derived Transition Metal Oxides and Composites as Anodes for Lithium-Ion Batteries. *Inorg. Chem. Front.* **2020**, *7*, 4939−4955.

(2) Cai, P.; Zou, K.; Zou, G.; Hou, H.; Ji, X. Quinone/Ester-Based Oxygen Functional Group-Incorporated Full Carbon Li-Ion Capacitor for Enhanced Performance. *Nanoscale* **2020**, *12*, 3677−3685.

(3) Chen, J.; Zou, G.; Deng, W.; Huang, Z.; Gao, X.; Liu, C.; Yin, S.; Liu, H.; Deng, X.; Tian, Y.; et al. Pseudo-Bonding and Electric-Field Harmony for Li-Rich Mn-Based Oxide Cathode. *Adv. Funct. Mater.* **2020**, *30*, 2004302.

(4) Huang, W.; Li, X.; Yang, X.; Zhang, X.; Wang, H. The Recent Progress and Perspectives on Metal-and Covalent-Organic Framework Based Solid-State Electrolytes for Lithium-Ion Batteries. *Mater. Chem. Front.* **2021**, *5*, 3593−3613.

(5) Wang, L.; Chen, B.; Ma, J.; Cui, G.; Chen, L. Reviving Lithium Cobalt Oxide-Based Lithium Secondary Batteries-Toward a Higher Energy Density. *Chem. Soc. Rev.* **2018**, *47*, 6505−6602.

(6) Lee, J.; Choi, C.; Kim, J.; de Andrade, M. J.; Baughman, R. H.; Kim, S. J. Biscrolled Carbon Nanotube Yarn Structured Silver-Zinc Battery. *Sci. Rep.* **2018**, *8*, 11150.

(7) Li, R.; Zhu, X.; Fu, Q.; Liang, G.; Chen, Y.; Luo, L.; Dong, M.; Shao, Q.; Lin, C.; Wei, R.; Guo, Z. Nanosheet-Based $Nb_{12}O_{29}$ Hierarchical Microspheres for Enhanced Lithium Storage. *Chem. Commun.* **2019**, *55*, 2493−2496.

(8) Qu, Z.; Shi, M.; Wu, H.; Liu, Y.; Jiang, J.; Yan, C. An Efficient Binder-Free Electrode with Multiple Carbonized Channels Wrapped by $NiCo_2O_4$ Nanosheets for High-Performance Capacitive Energy Storage. *J. Power Sources* **2019**, *410*, 179−187.

(9) Lou, X.; Lin, C.; Luo, Q.; Zhao, J.; Wang, B.; Li, J.; Shao, Q.; Guo, X.; Wang, N.; Guo, Z. Crystal Structure Modification Enhanced $Fenb_{11}O_{29}$ Anodes for Lithium-Ion Batteries. *ChemElectroChem* **2017**, *4*, 3171−3180.

(10) Li, T.; Bai, Y.; Wang, Y.; Xu, H.; Jin, H. Advances in Transition-Metal (Zn, Mn, Cu)-Based MOFs and Their Derivatives for Anode of Lithium-Ion Batteries. *Coord. Chem. Rev.* **2020**, *410*, 213221.

(11) Jin, J.; Wu, L.; Huang, S.; Yan, M.; Wang, H.; Chen, L.; Hasan, T.; Li, Y.; Su, B. Hierarchy Design in Metal Oxides as Anodes for Advanced Lithium-Ion Batteries. *Small Methods* **2018**, *2*, 1800171.

(12) Reddy, R. C. K.; Lin, J.; Chen, Y.; Zeng, C.; Lin, X.; Cai, Y.; Su, C. Progress of Nanostructured Metal Oxides Derived from Metal-Organic Frameworks as Anode Materials for Lithium-Ion Batteries. *Coord. Chem. Rev.* **2020**, *420*, 213434.

(13) Zheng, Z.; Wu, H. H.; Liu, H.; Zhang, Q.; He, X.; Yu, S.; Petrova, V.; Feng, J.; Kostecki, R.; Liu, P.; et al. Achieving Fast and Durable Lithium Storage through Amorphous FeP Nanoparticles Encapsulated in Ultrathin 3D P-Doped Porous Carbon Nanosheets. *ACS Nano* **2020**, *14*, 9545−9561.
(14) Li, Q.; Zhao, Y.; Liu, H.; Xu, P.; Yang, L.; Pei, K.; Zeng, Q.; Feng, Y.; Wang, P.; Che, R. Dandelion-Like Mn/Ni Co-Doped CoO/C Hollow Microspheres with Oxygen Vacancies for Advanced Lithium Storage. *ACS Nano* **2019**, *13*, 11921−11934.
(15) Bai, J.; Xi, B.; Mao, H.; Lin, Y.; Ma, X.; Feng, J.; Xiong, S. One-Step Construction of N, P-Codoped Porous Carbon Sheets/CoP Hybrids with Enhanced Lithium and Potassium Storage. *Adv. Mater.* **2018**, *30*, 1802310.
(16) Wu, C.; Kopold, P.; van Aken, P. A.; Maier, J.; Yu, Y. High Performance Graphene/Ni_2P Hybrid Anodes for Lithium and Sodium Storage through 3D Yolk-Shell-Like Nanostructural Design. *Adv. Mater.* **2017**, *29*, 1604015.
(17) Li, S.; Lin, J.; Xiong, W.; Guo, X.; Wu, D.; Zhang, Q.; Zhu, Q.; Zhang, L. Design Principles and Direct Applications of Cobalt-Based Metal-Organic Frameworks for Electrochemical Energy Storage. *Coord. Chem. Rev.* **2021**, *438*, 213872.
(18) Cai, G.; Yan, P.; Zhang, L.; Zhou, H.; Jiang, H. Metal-Organic Framework-Based Hierarchically Porous Materials: Synthesis and Applications. *Chem. Rev.* **2021**, *121*, 12278−12326.
(19) Yaghi, O. M.; Li, H. Hydrothermal Synthesis of a Metal-organic Framework Containing Large Rectangular Channels. *J. Am.Chem. Soc.* **1995**, *117*, 10401−10402.
(20) Li, Y.; Tong, Y.; Peng, F. Metal-Free Carbocatalysis for Electrochemical Oxygen Reduction Reaction: Activity Origin and Mechanism. *J. Energy Chem.* **2020**, *48*, 308−321.
(21) Chen, L.; Xu, Q. Metal-Organic Framework Composites for Catalysis. *Matter* **2019**, *1*, 57−89.
(22) Zheng, J.; Cui, X.; Yang, Q.; Ren, Q.; Yang, Y.; Xing, H. Shaping of Ultrahigh-Loading MOF Pellet with a Strongly Anti-Tearing Binder for Gas Separation and Storage. *Chem. Eng. J.* **2018**, *354*, 1075−1082.
(23) Yao, M.; Tang, W.; Wang, G.; Nath, B.; Xu, G. MOF Thin Film-Coated Metal Oxide Nanowire Array: Significantly Improved Chemiresistor Sensor Performance. *Adv. Mater.* **2016**, *28*, 5229−5234.
(24) Drobek, M.; Kim, J. H.; Bechelany, M.; Vallicari, C.; Julbe, A.; Kim, S. S. MOF-Based Membrane Encapsulated ZnO Nanowires for Enhanced Gas Sensor Selectivity. *ACS Appl. Mater. Interfaces* **2016**, *8*, 8323−8328.
(25) Zhu, X.; Zhang, K.; Wang, Y.; Long, W.; Sa, R.; Liu, T.; Lu, J. Fluorescent Metal-Organic Framework (MOF) as a Highly Sensitive and Quickly Responsive Chemical Sensor for the Detection of Antibiotics in Simulated Wastewater. *Inorg. Chem.* **2018**, *57*, 1060−1065.
(26) Wu, M.; Yang, Y. Metal-Organic Framework (MOF)-Based Drug/Cargo Delivery and Cancer Therapy. *Adv. Mater.* **2017**, *29*, 1606134.
(27) Shen, K.; Chen, X.; Chen, J.; Li, Y. Development of MOF-Derived Carbon-Based Nanomaterials for Efficient Catalysis. *ACS Catal.* **2016**, *6*, 5887−5903.
(28) Wen, X.; Zhang, Q.; Guan, J. Applications of Metal-Organic Framework-Derived Materials in Fuel Cells and Metal-Air Batteries. *Coord. Chem. Rev.* **2020**, *409*, 213214.
(29) Cherusseri, J.; Pandey, D.; Kumar, K. S.; Thomas, J.; Zhai, L. Flexible Supercapacitor Electrodes Using Metal-Organic Frameworks. *Nanoscale* **2020**, *12*, 17649−17662.
(30) Dou, J.; Zhu, C.; Wang, H.; Han, Y.; Ma, S.; Niu, X.; Li, N.; Shi, C.; Qiu, Z.; Zhou, H.; et al. Synergistic Effects of Eu-MOF on Perovskite Solar Cells with Improved Stability. *Adv. Mater.* **2021**, *33*, 2102947.
(31) De Combarieu, G.; Morcrette, M.; Millange, F.; Guillou, N.; Cabana, J.; Grey, C. P.; Margiolaki, I.; Férey, G.; Tarascon, J. M. Influence of the Benzoquinone Sorption on the Structure and Electrochemical Performance of the MIL-53 (Fe) Hybrid Porous Material in a Lithium-Ion Battery. *Chem. Mater.* **2009**, *21*, 1602−1611.
(32) Zhang, L.; Liu, H.; Shi, W.; Cheng, P. Synthesis Strategies and Potential Applications of Metal-Organic Frameworks for Electrode Materials for Rechargeable Lithium Ion Batteries. *Coord. Chem. Rev.* **2019**, *388*, 293−309.
(33) Chen, L.; Yang, W.; Wang, J.; Chen, C.; Wei, M. Hierarchical Cobalt-Based Metal-Organic Framework for High-Performance Lithium-Ion Batteries. *Chemistry* **2018**, *24*, 13362−13367.
(34) Shrivastav, V.; Sundriyal, S.; Goel, P.; Kaur, H.; Tuteja, S. K.; Vikrant, K.; Kim, K.-H.; Tiwari, U. K.; Deep, A. Metal-Organic Frameworks (MOFs) and Their Composites as Electrodes for Lithium Battery Applications: Novel Means for Alternative Energy Storage. *Coord. Chem. Rev.* **2019**, *393*, 48−78.
(35) Sun, W.; Cai, C.; Tang, X.; Lv, L.; Wang, Y. Carbon Coated Mixed-Metal Selenide Microrod: Bimetal-Organic-Framework Derivation Approach and Applications for Lithium-Ion Batteries. *Chem. Eng. J.* **2018**, *351*, 169−176.
(36) Raza, N.; Kumar, T.; Singh, V.; Kim, K. Recent Advances in Bimetallic Metal-Organic Framework as a Potential Candidate for Supercapacitor Electrode Material. *Coord. Chem. Rev.* **2021**, *430*, 213660.
(37) Liang, Q.; Chen, J.; Wang, F.; Li, Y. Transition Metal-Based Metal-Organic Frameworks for Oxygen Evolution Reaction. *Coord. Chem. Rev.* **2020**, *424*, 213488.
(38) Lou, X.; Ning, Y.; Li, C.; Hu, X.; Shen, M.; Hu, B. Bimetallic Zeolite Imidazolate Framework for Enhanced Lithium Storage Boosted by the Redox Participation of Nitrogen Atoms. *Sci. China Mater.* **2018**, *61*, 1040−1048.
(39) Jin, J.; Zheng, Y.; Huang, S.; Sun, P.; Srikanth, N.; Kong, L.; Yan, Q.; Zhou, K. Directly Anchoring 2D NiCo Metal-Organic Frameworks on Few-Layer Black Phosphorus for Advanced Lithium-Ion Batteries. *J. Mater. Chem. A* **2019**, *7*, 783−790.
(40) Kim, H. T.; Kim, J. K.; Cha, H. G.; Kang, M. J.; Lee, H. S.; Khang, T. U.; Yun, E. J.; Lee, D.; Song, B. K.; Park, S. J.; Joo, J. C.; Kim, K. H. Biological Valorization of Poly (Ethylene Terephthalate) Monomers for Upcycling Waste PET. *ACS Sustainable Chem. Eng.* **2019**, *7*, 19396−19406.
(41) Geueke, B.; Groh, K.; Muncke, J. Food Packaging in the Circular Economy: Overview of Chemical Safety Aspects for Commonly Used Materials. *J. Cleaner Prod.* **2018**, *193*, 491−505.
(42) Bascucci, C.; Duretek, I.; Lehner, S.; Holzer, C.; Gaan, S.; Hufenus, R.; Gooneie, A. Investigating Thermomechanical Recycling of Poly (Ethylene terephthalate) Containing Phosphorus Flame Retardants. *Polym. Degrad. Stab.* **2022**, *195*, 109783.
(43) Li, Y.; Chen, J.; Han, W.; Yi, H.; Wang, J.; Xing, P.; Ren, J.; Yao, D. Toward Making Poly (Ethylene Terephthalate) Degradable in Aqueous Environment. *Macromol. Mater. Eng.* **2022**, *307*, 2100832.
(44) Jiang, J.; Shi, K.; Zhang, X.; Yu, K.; Zhang, H.; He, J.; Ju, Y.; Liu, J. From Plastic Waste to Wealth Using Chemical Recycling: A Review. *J. Environ. Chem. Eng.* **2022**, *10*, 106867.
(45) Yong, C. Q. Y.; Valiyaveettil, S.; Tang, B. L. Toxicity of Microplastics and Nanoplastics in Mammalian Systems. *Int. J. Environ. Res. Public Health* **2020**, *17*, 1509.
(46) Vanapalli, K. R.; Sharma, H. B.; Ranjan, V. P.; Samal, B.; Bhattacharya, J.; Dubey, B. K.; Goel, S. Challenges and Strategies for Effective Plastic Waste Management During and Post COVID-19 Pandemic. *Sci. Total Environ.* **2021**, *750*, 141514.
(47) Ghosh, A.; Das, G. Facile Synthesis of Sn(II)-MOF Using Waste Pet Bottles as an Organic Precursor and Its Derivative SnO_2 Nps: Role of Surface Charge Reversal in Adsorption of Toxic Ions. *J. Environ. Chem. Eng.* **2021**, *9*, 105288.
(48) Dyosiba, X.; Ren, J.; Musyoka, N. M.; Langmi, H. W.; Mathe, M.; Onyango, M. S. Feasibility of Varied Polyethylene Terephthalate Wastes as a Linker Source in Metal-Organic Framework Uio-66 (Zr) Synthesis. *Ind. Eng. Chem. Res.* **2019**, *58*, 17010−17016.
(49) Jung, K.; Kim, J.; Choi, J. Synthesis of Magnetic Porous Carbon Composite Derived from Metal-Organic Framework Using Recovered Terephthalic Acid from Polyethylene Terephthalate (PET) Waste

https://doi.org/10.1021/acsomega.2c04264
ACS Omega 2022, 7, 35180−35190

Bottles as Organic Ligand and Its Potential as Adsorbent for Antibiotic Tetracycline Hydrochloride. *Composites, Part B* **2020**, *187*, 107867.
(50) Lu, X.; Zhao, C. Electrodeposition of Hierarchically Structured Three-Dimensional Nickel-Iron Electrodes for Efficient Oxygen Evolution at High Current Densities. *Nat. Commun.* **2015**, *6*, 1−7.
(51) Mutahir, S.; Wang, C.; Song, J.; Wang, L.; Lei, W.; Jiao, X.; Khan, M. A.; Zhou, B.; Zhong, Q.; Hao, Q. Pristine Co(BDC)$TED_{0.5}$ a Pillared-Layer Biligand Cobalt Based Metal Organic Framework as Improved Anode Material for Lithium-Ion Batteries. *Applied. Mater. Today* **2020**, *21*, 100813.
(52) Zhao, S.; Wang, Y.; Dong, J.; He, C.; Yin, H.; An, P.; Zhao, K.; Zhang, X.; Gao, C.; Zhang, L.; et al. Ultrathin Metal-Organic Framework Nanosheets for Electrocatalytic Oxygen Evolution. *Nat. Energy* **2016**, *1*, 1−10.
(53) Singh, S.; Sharma, S.; Umar, A.; Jha, M.; Mehta, S. K.; Kansal, K. S. Nanocuboidal-Shaped Zirconium Based Metal Organic Framework for the Enhanced Adsorptive Removal of Nonsteroidal Anti-Inflammatory Drug. *New J. Chem.* **2018**, *42*, 1921−1930.
(54) Ye, C.; Qin, Q.; Liu, J.; Mao, W.; Yan, J.; Wang, Y.; Cui, J.; Zhang, Q.; Yang, L.; Wu, Y. Coordination Derived Stable Ni-Co MOFs for Foldable All-Solid-State Supercapacitors with High Specific Energy. *J. Mater. Chem. A* **2019**, *7*, 4998−5008.
(55) Hu, X.; Hu, H.; Li, C.; Li, T.; Lou, X.; Chen, Q.; Hu, B. Cobalt-Based Metal Organic Framework with Superior Lithium Anodic Performance. *J. Solid State Chem.* **2016**, *242*, 71−76.
(56) Li, C.; Lou, X.; Yang, Q.; Zou, Y.; Hu, B. Remarkable Improvement in the Lithium Storage Property of $Co_2(OH)_2$BDC MOF by Covalent Stitching to Graphene and the Redox Chemistry Boosted by Delocalized Electron Spins. *Chem. Eng. J.* **2017**, *326*, 1000−1008.
(57) Gong, T.; Lou, X.; Gao, E. Q.; Hu, B. Pillared-Layer Metal-Organic Frameworks for Improved Lithium-Ion Storage Performance. *ACS Appl. Mater. Interfaces* **2017**, *9*, 21839−21847.
(58) Yang, Z.; Shen, X.; Wang, N.; He, J.; Li, X.; Wang, X.; Hou, Z.; Wang, K.; Gao, J.; Jiu, T.; et al. Graphdiyne Containing Atomically Precise N Atoms for Efficient Anchoring of Lithium Ion. *ACS Appl. Mater. Interfaces* **2019**, *11*, 2608−2617.
(59) Kim, H.; Choi, W.; Yoon, J.; Um, J. H.; Lee, W.; Kim, J.; Cabana, J.; Yoon, W. S. Exploring Anomalous Charge Storage in Anode Materials for Next-Generation Li Rechargeable Batteries. *Chem. Rev.* **2020**, *120*, 6934−6976.

https://doi.org/10.1021/acsomega.2c04264
ACS Omega 2022, 7, 35180−35190